Research in Astronomy and Astrophysics, 23:035015 (15pp), 2023 March https://doi.org/10.1088/1674-4527/acb9db

Discrepancy in Grain Size Estimation of H_2O Ice in the Outer Solar System

A. Emran[1] and V. F. Chevrier
Space and Planetary Sciences, University of Arkansas, Fayetteville, AR 72701, USA; al.emran@jpl.nasa.gov
Received 2022 October 21; revised 2023 January 6; accepted 2023 January 12; published 2023 March 10

Abstract

Radiative transfer models (RTMs) have been used to estimate grain size of amorphous and crystalline water (H_2O) ice in the outer solar system from near-infrared (NIR) wavelengths. We use radiative scattering models to assess the discrepancy in grain size estimation of H_2O ice at a temperature of 15, 40, 60, and 80 K (amorphous) and 20, 40, 60, and 80 K (crystalline)—relevant to the outer solar system. We compare the single scattering albedos of H_2O ice phases using the Mie theory and Hapke approximation models from the optical constant at NIR wavelengths (1–5 μm). This study reveals that Hapke approximation models—Hapke slab and internal scattering model (ISM)—predict grain size of crystalline phase slightly closer to Mie model than amorphous phase at temperatures of 15–80 K. However, the Hapke slab model predicts, in general, grain sizes much closer to those of the Mie model's estimations while ISM predicted grain sizes exhibit a higher uncertainty. We recommend using the Mie model for unknown spectra of outer solar system bodies to estimate H_2O ice grain sizes. While choosing the approximation model for employing RTMs, we recommend using a Hapke slab approximation model over the ISM.

Key words: Kuiper Belt: general – planets and satellites: fundamental parameters – techniques: spectroscopic – scattering – radiative transfer

1. Introduction

Detection of water (H_2O) ice has previously been established on outer solar system bodies (giant planets' rings and their icy moons and dwarf planets), cometary bodies (originating from the Kuiper Belt and Oort cloud), and interstellar medium (see Kofman et al. 2019 for an exhaustive list of references). Solid H_2O ice in the solar system may appear as crystalline, amorphous, or both based on temperature, radiation history, and formation temperature and pressure conditions (Cruikshank et al. 1998; Schmitt et al. 1998; Mastrapa et al. 2008). Though amorphous water ice (microporous amorphous phase) is considered the most abundant form of H_2O in the universe (Baragiola 2003), the crystalline phase has also been spotted in many outer solar system bodies.

Phases of amorphous and crystalline H_2O ice were investigated on the Galilean moons of Jupiter using data from the NIMS instrument onboard the Galileo spacecraft (Hansen & McCord 2004). Neptune's moon Triton, a trans-Neptunian object (TNO), is also assumed to host amorphous and crystalline water ice (Cruikshank et al. 2000). Although the presence of crystalline H_2O ice has been reported on Pluto's surface (Cook et al. 2019; Emran et al. 2023), its largest satellite Charon may host both amorphous and crystalline H_2O phases (Dalle Ore et al. 2018). Molecules of amorphous H_2O ice have been detected on icy dust grains in dense interstellar clouds (e.g., Herbst 2001). Due to the formation of cometary icy grains at very low temperatures, the water ice within cometesimals is thought to be in an amorphous phase (Raponi et al. 2016).

Observations from different spectral wavelengths are used to study the outer reaches of the solar system. Among the wavelengths, the near-infrared (NIR, typically 0.8–5 μm wavelength) has the most diagnostic bands and therefore has been extensively used for characterizing ices and volatiles on outer solar system bodies (Barucci & Merlin 2020). The interactions between infrared photons and H_2O ices and their resultant absorption bands and positions are dependent on its crystalline versus amorphous phases and the temperature of the ice (Mastrapa et al. 2009). Thus, the shapes and position of the infrared absorption bands and their variations in response to temperature are considered when diagnosing astronomical ices (e.g., Schmitt et al. 1998). At NIR wavelengths, amorphous water ice exhibits different spectral characteristics (i.e., the shape of the absorption bands) above and below the temperature of 70 K (Mastrapa et al. 2008). Water ice in the outer solar system can be identified using the characteristic absorption bands at 1.5, 1.65, 2.0, and ~3.1 μm. However, crystalline H_2O ice shows a stronger absorption at 1.65 μm compared to amorphous H_2O ice (Mastrapa et al. 2008). The 3.1 μm absorption band (or Fresnel Peak) for crystalline H_2O ice consists of three separate absorption features at ~3.2, ~3.1, and ~3.0 μm (Mastrapa et al. 2009). In contrast, amorphous

[1] Now at NASA Jet Propulsion Laboratory, California Institute of Technology, Pasadena, CA 91109. This work was done as a private venture and not in the author's capacity as an employee of the Jet Propulsion Laboratory, California Institute of Technology.

H_2O ice exhibits one broad absorption band near 3.1 μm (Mastrapa et al. 2009). While crystalline and amorphous H_2O ice shows a much larger difference at low temperatures, the difference decreases with temperature (Mastrapa et al. 2008, 2009).

Radiative transfer models (RTMs) have been used to characterize the composition of outer solar system bodies such as Kuiper Belt objects (KBOs) and TNOs (e.g., Grundy & Fink 1991; Dumas et al. 2007; Merlin et al. 2010; Tegler et al. 2010). However, wide discrepancies in the estimation of grain size have been reported for H_2O ice on Saturnian moons such as Enceladus (Hansen 2009), as well as nitrogen (N_2) and methane (CH_4) ices on TNOs and KBOs using different scattering models (Emran & Chevrier 2022). These uncertainties are believed to arise due to the use of different single scattering albedo (w) calculations rather than a choice of using bidirectional scattering models (Hansen 2009). Accordingly, Hansen (2009) compared the single scattering albedos using the optical constant data of crystalline H_2O ice at 110 K—relevant to Saturnian moons and other icy bodies. However, temperatures at the far reaches of the solar system at the TNO and the Kuiper Belt are much lower, and amorphous ice should dominate these environments. For instance, Pluto has a maximum global temperature of 37.7 K in its current epoch (Earle et al. 2017).

Furthermore, while employing RTMs in the outer solar system bodies, there has been extensive use of optical constants of crystalline and/or amorphous phases of H_2O ice and a variety of scattering models. For instance, Protopapa et al. (2017) considered the optical constant of crystalline H_2O ice and employed the equivalent slab model of Hapke (1993) for mapping the spatial distribution and grain size of water ice (along with other ices) on Pluto. For the same planetary body, Cook et al. (2019) utilized the optical constant of both amorphous and crystalline ices while their scattering model was following the formulations of Roush (1994) and Cruikshank et al. (1998) with some modifications. Because w is the primary cause of discrepancies in the grain size estimation of ices (Hansen 2009; Emran & Chevrier 2022), the uncertainty of the grain size estimation of amorphous and crystalline H_2O ice, at temperatures analogous to the outer solar system (i.e., 15–80 K), using different scattering models is warranted.

We assess the uncertainty in predicting the H_2O ice grain sizes at a temperature of 15, 40, 60, and 80 K (amorphous) and 20, 40, 60, and 80 K (crystalline) analogous to the outer solar system bodies including the TNOs and KBOs. The theory of Mie (1908) and approximation models of Hapke (1993) are commonly used methods for calculating the w of a material from its optical constants. Accordingly, we calculate the w of water (amorphous and crystalline) ices by implementing Mie theory and the widely used Hapke approximation models from the optical constants over the wavelengths between 1 and 5 μm. We follow that up by comparing the relative grain sizes of amorphous and crystalline H_2O ice predicted by the approximation models to the Mie model.

2. Methods

2.1. Optical Constants

We use the NIR optical constants of H_2O ice at a temperature of 15–80 K (amorphous phase) and 20–80 K (crystalline phase). The optical constants of amorphous and crystalline ice at NIR wavelengths between 1.1 and 2.6 μm were prepared by Mastrapa et al. (2008) and NIR to mid-infrared wavelengths between 2.5 and 22 μm by Mastrapa et al. (2009). A compiled set of optical constant data for both ice phases over the entire NIR wavelengths (1–5 μm)—used in this study—can be found in Mastrapa et al. (2009). Note that the crystalline phase used in this study is assumed to be the cubic ice form—a meta-stable H_2O ice phase (Mastrapa et al. 2009). The cubic and hexagonal crystalline ices exhibit nearly identical spectra at infrared wavelengths (Bertie & Whalley 1967). Thus, in this study, we do not distinguish cubic versus hexagonal ice, but rather we treat the crystalline phases as a unified entity. We regard the cubic ice as the representative of crystalline ice, and hereafter, we denote the crystalline ice as Ic and amorphous ice as Ia.

We use the optical constant data from Mastrapa et al. (2008, 2009) to maintain consistency across the entire wavelength range since the samples used to determine the parameters were prepared utilizing the same instrumental setup, although there are other sources of optical constants for water ice. For instance, Grundy & Schmitt (1998) prepared the optical constants for monocrystalline (hexagonal) H_2O ice samples between the wavelengths of 0.97–2.73 μm at temperatures of 20–270 K. On the other hand, Hudgins et al. (1993) prepared the optical constants of ice Ia between the wavelengths of 2.5–20 μm at temperatures of 10–120 K.

2.2. Single Scattering Albedo

Photon interaction with a material grain happens at the atomic-molecular level through the process of selective absorption, emission, and scattering (e.g., Shepard 2017). The sum of scattering and absorption efficiencies of a particle, at a given wavelength, by its physical cross-section is called extinction efficiency, $Q_{\rm ext} = Q_{\rm sc} + Q_{\rm ab}$. The w is the ratio of scattering efficiency and extinction efficiency, $w = Q_{\rm sc}/Q_{\rm ext}$.

For planetary regolith, w is a representative of characteristic surface properties including grain size, optical properties, internal structure, and partly shapes (Hapke 1981). Consequently, the grain size estimation of the regolith primarily depends on the characteristic value of w by the surface particles (Hansen 2009). A material's w is a function of optical properties (indices of refraction) of its single grain (e.g., Hapke 1993; Mustard & Glotch 2019). Thus, w can be calculated if

optical constants—both real (n) and imaginary (k) parts—of the regolith medium are known. Larger particles with moderate to larger k values result in higher absorption of incident light and, therefore, are associated with a lower w value (e.g., Shepard & Helfenstein 2007).

Mie scattering theory can accurately estimate the w for a particle with a spherical shape (Mie 1908). That means Mie's theory (Mie 1908) can accurately calculate the scattering properties of uniform (shaped) particles. Further, besides application to scattering properties for the equant particles of Mie spheres, the Mie scattering model has been devised to be satisfactorily employed for particles with varied "equivalent" non-spherical shapes if each non-spherical particle can be represented by assemblages of spheres with the same volume-to-surface-area ratio as the non-spherical particle (e.g., Grenfell & Warren 1999; Grenfell et al. 2005). In other words, roughly similar scattering properties have been reported regarding irregular particles to scattering properties calculated by similar-sized spherical particles using Mie's theory (Hapke 1981). This implies that the scattering properties of Mie theory for spherical particles can be mimicked by irregular particles (Neshyba et al. 2003), and thus application to Mie theory in the grain size estimation of a Mie's equant particle is somewhat analogous to non-spherical/irregular grains (e.g., Hapke 1981; Hansen 2009).

On the other hand, Hapke (1993) formulates a variety of approximation models for the estimation of w from material optical constants. We employ two of these approximation models—the "*espat*" slab (hereafter the Hapke slab or simply slab model; Hapke 1981, 1993) and a version of the internal scattering model (ISM; Hapke 1993)—which have widely been used in the RTMs of the outer solar system bodies. Note that the version of the scattering model by Roush (1994) uses, indeed, a formulation of the ISM in the original paper by Hapke (1981) and devised the versions of surface scattering functions (Hansen 2009). Mie's theory appropriately accounts for the Rayleigh effect on the single scattering albedo that happens to grain size close to the wavelengths. However, Hapke approximation models have a shortcoming such that neither of the models accounts for the Rayleigh effects on single scattering albedo. Consequently, the calculated w using the approximation models is deviant from that of the Mie model (Hansen 2009). Accordingly, for the implementation of RTMs, Hansen (2009) and Emran & Chevrier (2022) recommend using the Mie theory for a spectrum of outer solar system bodies. In this research, therefore, the deviation of estimated grain sizes by the approximation models to Mie's prediction is labeled as the discrepancy in grain size estimation by the approximation models throughout the paper.

2.3. Mie Calculation

The scattering properties of a particle with the simplest three-dimensional geometrics (spheres) can accurately be calculated using the Mie theory by employing Maxwell's equations (Mie 1908; Wiscombe 1980). The formulation of the Mie theory accounts for optical constants ($n + ik$) of the particle and the fraction of the particle's size to wavelengths under investigation (Hapke 1993). However, the treatment of diffraction effects in Mie's w is required for a scattering model with highly asymmetric phase functions (Hansen 2009). Thus, in this study we use δ–Eddington corrected (Joseph et al. 1976) Mie single scattering albedo, w', calculated as (Wiscombe & Warren 1980)

$$w' = \frac{(1 - \xi^2)\, w}{1 - \xi^2 w}, \tag{1}$$

where ξ is the asymmetry factor calculated by Mie theory. Following the approach of Emran & Chevrier (2022), the Mie w was calculated by utilizing the method of Wiscombe (1979) using the `miepython` routine (an open-source Python module). The δ–Eddington corrected Mie w' was then adjusted from Mie's w following Equation (1).

2.4. Hapke Approximation Models

Using the "*espat*" function or the slab model of Hapke (1981, 1993), the approximate w of an equant particle can be simplified as

$$w = \frac{1}{\alpha D_e + 1}, \tag{2}$$

where α is the absorption coefficient and D_e is the "effective particle size." The absorption coefficient is given by

$$\alpha = \frac{4\pi k}{\lambda}, \tag{3}$$

where k is the imaginary part of the optical constant and λ is the wavelength under consideration. The Hapke slab model should be applied for materials with $k \ll 1$ and D_e can be approximated as (Hapke 1993)

$$D_e = \hat{g}\frac{1 - S_e}{1 - S_i} D, \tag{4}$$

where D is the particle diameter, $\hat{g}$ is a constant (scaling parameter of diameter) which is roughly $= 1$, and S_e and S_i are the average Fresnel reflection coefficient for externally and internally incident light, respectively. The derivations of the approximate equations for the calculation of S_e and S_i are given in Hapke (1993) where k is set to be zero, and therefore is not considered, for the slab model. These approximate equations (S_e and S_i) can also be found elsewhere in the literature that uses the Hapke models including the study of Emran & Chevrier (2022). The calculation of w using the ISM can be approximated as (Hapke 1993)

$$w = S_e + (1 - S_e)\frac{(1 - S_i)\Theta}{1 - S_i\Theta}, \tag{5}$$

where particles' internal-transmission function Θ is given by Hapke (1993)

$$\Theta = \frac{r + \exp(-\sqrt{(\alpha(\alpha+s))}\langle D\rangle}{1 - r\,\exp(-\sqrt{(\alpha(\alpha+s))}\langle D\rangle}, \quad (6)$$

and s is the near-surface internal scattering coefficient. The mean free path of photon $\langle D\rangle$ as a function of n for a perfectly spherical particle can be written as (Hapke 1993)

$$\langle D\rangle = \frac{2}{3}\left(n^2 - \frac{1}{n}(n^2-1)^{\frac{3}{2}}\right)D. \quad (7)$$

The internal hemispherical (diffused) reflectance r can be expressed as (Hapke 1981)

$$r = \frac{1 - \sqrt{\alpha(\alpha+s)}}{1 + \sqrt{\alpha(\alpha+s)}}. \quad (8)$$

If s is set to zero (Lucey 1998), then r=0 and $\Theta = e^{-\alpha\langle D\rangle}$ (e.g., Lawrence & Lucey 2007; Hansen 2009; Li & Li 2011). The list of notations used in this study is given in Appendix B.

As seen in the equations above, an obvious difference between the ISM and the slab models is the calculation of average Fresnel reflection coefficients—the former model employs data from both n and k parts while the latter uses only the n part of the refractive indices. Since the slab model can be applied when k is very small (Hapke 1981, 1993), wavelengths with a substantially higher k value can lead to a higher difference in calculated w between the approximation models. Note that if the approximation model assumes the internal scattering coefficient $s = 0$ (as used by many existing studies, for example, Lucey 1998; Lawrence & Lucey 2007) then the internal diffused reflectance r equals zero as well. However, Sharkey et al. (2019) expressed the relationship between the s and D ("effective diameter") as $s = 1/D$ and the number of scattering events $(sD) = 1$ within a single grain. Thus, this relationship indicates that s cannot be zero (Emran & Chevrier 2022).

3. Results

3.1. Calculated Single Scattering Albedo

We compare the w spectra of 10 μm radii Ia and Ic particles to assess the difference in calculated single scattering albedo at that specific diameter using the Mie and Hapke approximation models over the NIR range (Figure 1). Following the approach of Emran & Chevrier (2022), we apply the Savitzky–Golay filter (Savitzky & Golay 1964) to smoothen the small spikes in calculated w curves over the wavelength range. We implement the filter algorithm with a 3rd order polynomial fit. Note that all plots used in this study were smoothened using the Savitzky–Golay filter, if not mentioned otherwise.

The w plots from the Hapke approximation models follow the spectra generated by the Mie model with varying degrees of closeness at different NIR wavelengths. In the case of Ia at every investigated temperature (left column in Figure 1), the Hapke slab model provides a much better approximation of the Mie model spectra compared to the ISM spectra, except around the broader 3.0 μm region. At shorter wavelengths up to 2.5 μm, the slab model produces slightly higher w values than the Mie model, notably around the weak overtones at 1.5 and 2.0 μm at every investigated temperature. This represents a prediction of a slightly smaller H_2O grain size by the slab model compared to the Mie model (Hansen 2009) over the shorter wavelengths.

The w spectra of Ia at the broader 4.5 μm absorption band show that the slab model either exactly reproduces the Mie spectra (at 15 K) or renders slightly higher w values than the Mie spectra (at 40, 60, and 80 K). This indicates that the slab model predicts identical or slightly smaller grain sizes than Mie's prediction. In contrast, at every temperature, the ISM renders much lower w than the Mie spectra at the 4.5 μm band—indicating a larger grain size prediction by the ISM. At the wavelengths around 3.5 and 5 μm, both approximation models show smaller w values than the Mie model—meaning a larger grain size prediction by the approximation models at these bands. However, the grain size prediction by the approximation models is much larger at 5 μm than that at 3.5 μm.

In the instance of Ic at every investigated temperature (right column in Figure 1), the slab model almost accurately reproduces the Mie model for the weak overtone at 1.5 μm while it shows slightly higher w values for the weak overtone at 2.0 μm. This represents an accurate grain size prediction at 1.5 μm and a slightly smaller grain size prediction at 2.0 μm by the slab model. The ISM, on the other hand, predicts much smaller grain sizes than the Mie model at both 1.5 and 2.0 μm. At the broader 4.4 μm absorption band of Ic, the slab model predicts smaller grain sizes while the ISM model predicts larger grain sizes compared to Mie's prediction—because the calculated w values by the slab model and ISM at the wavelength region are higher and lower, respectively than the Mie model. Both the approximation models follow the same path and show much smaller w values at the 3.5 and 5 μm bands—indicating a much larger grain size prediction by the approximation models at these bands. However, the differences between spectra of the Hapke approximations and Mie models at 3.5 μm are much higher for Ic compared to Ia at every investigated temperature (see the left and right columns of Figure 1).

Though the ISM spectra can reproduce the 3.1 μm reflection peak of Ia at lower temperatures (e.g., 15 and 40 K), it partially reproduces the reflection peak at higher temperatures (e.g., 80 K); whereas the slab model fails to reproduce the 3.1 μm reflection peak of Ia at every temperature. The 3.1 μm reflection peak of Ic is much sharper and slightly redshifted than ice Ia. Neither of the approximation models reproduces the 3.1 μm reflection peak of Ic at any investigated temperatures.

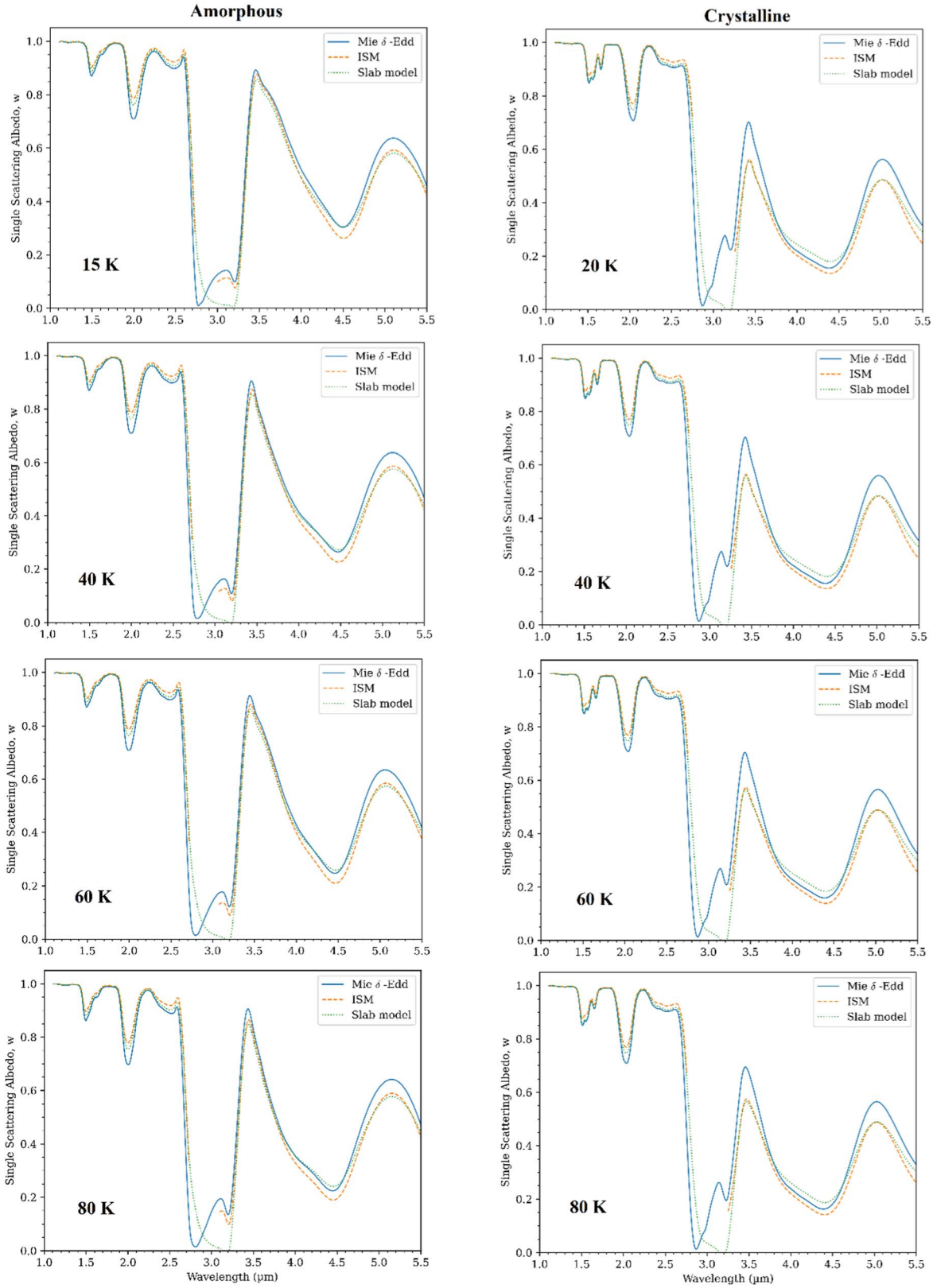

Figure 1. Calculated single scattering albedo plots for 10 μm radii particles of amorphous (left column) and crystalline (right column) H_2O ice at the NIR wavelengths. The subplots in the rows are the measurements at different temperatures where blue solid lines are δ–Eddington corrected Mie, green dotted lines are Hapke slab, and yellow dashed lines are ISM spectra.

Table 1

The Statistics—Medians and their 16% Quantile as a Lower 1σ Error Bar and 84% Quantile as an Upper 1σ Error Bar—of Relative Discrepancies in Predicted Grain Sizes using the Hapke Slab and ISM Calculated at Particle Radii of 1, 10, 100, and 1000 μm for Amorphous (a) and Crystalline (b) H_2O ice at Different Temperatures

a.

Grain Radii (μm)	Amorphous H_2O ice[a]							
	15 K		40 K		60 K		80 K	
	Slab	ISM	Slab	ISM	Slab	ISM	Slab	ISM
1	$1.07^{+1.04}_{-0.25}$	$1.28^{+1.08}_{-0.29}$	$1.07^{+0.97}_{-0.25}$	$1.28^{+1.02}_{-0.29}$	$1.07^{+0.96}_{-0.25}$	$1.29^{+1.04}_{-0.30}$	$1.08^{+0.92}_{-0.26}$	$1.29^{+1.03}_{-0.30}$
10	$1.19^{+0.06}_{-0.34}$	$1.44^{+0.05}_{-0.56}$	$1.20^{+0.07}_{-0.29}$	$1.45^{+0.05}_{-0.57}$	$1.21^{+0.06}_{-0.31}$	$1.46^{+0.05}_{-0.58}$	$1.21^{+0.06}_{-0.26}$	$1.46^{+0.05}_{-0.58}$
100	$1.46^{+0.58}_{-0.12}$	$1.66^{+0.35}_{-0.10}$	$1.46^{+0.58}_{-0.26}$	$1.66^{+0.48}_{-0.09}$	$1.47^{+0.62}_{-0.26}$	$1.67^{+0.45}_{-0.09}$	$1.47^{+0.60}_{-0.35}$	$1.67^{+0.51}_{-0.09}$
1000	$1.54^{+1.08}_{-1.37}$	$1.67^{+4.34}_{-1.08}$	$1.54^{+1.09}_{-1.38}$	$1.67^{+4.34}_{-1.19}$	$1.55^{+1.11}_{-1.37}$	$1.68^{+4.35}_{-1.23}$	$1.55^{+1.10}_{-1.40}$	$1.68^{+3.87}_{-1.26}$

b.

Grain Radii (μm)	Crystalline H_2O ice[a]							
	20 K		40 K		60 K		80 K	
	Slab	ISM	Slab	ISM	Slab	ISM	Slab	ISM
1	$0.88^{+0.67}_{-0.19}$	$1.03^{+0.76}_{-0.22}$	$0.87^{+0.67}_{-0.19}$	$1.03^{+0.76}_{-0.22}$	$0.88^{+0.67}_{-0.19}$	$1.03^{+0.75}_{-0.22}$	$0.87^{+0.67}_{-0.19}$	$1.03^{+0.75}_{-0.22}$
10	$1.10^{+0.08}_{-0.07}$	$1.30^{+0.07}_{-0.44}$	$1.09^{+0.07}_{-0.06}$	$1.30^{+0.07}_{-0.44}$	$1.09^{+0.07}_{-0.07}$	$1.30^{+0.07}_{-0.44}$	$1.09^{+0.07}_{-0.07}$	$1.30^{+0.07}_{-0.44}$
100	$1.24^{+0.65}_{-0.54}$	$1.46^{+0.40}_{-0.03}$	$1.24^{+0.65}_{-0.54}$	$1.46^{+0.40}_{-0.03}$	$1.25^{+0.64}_{-0.51}$	$1.46^{+0.41}_{-0.03}$	$1.24^{+0.64}_{-0.51}$	$1.46^{+0.41}_{-0.03}$
1000	$1.34^{+0.80}_{-1.27}$	$1.47^{+3.57}_{-1.25}$	$1.34^{+0.81}_{-1.27}$	$1.47^{+3.64}_{-1.25}$	$1.34^{+0.81}_{-1.26}$	$1.47^{+3.78}_{-1.24}$	$1.34^{+0.81}_{-1.26}$	$1.47^{+3.78}_{-1.24}$

Note.

[a] The statistics were computed by normalizing the estimated grain sizes from the Hapke slab and ISM to the Mie grain size. The number values are the medians and their 16% quantile as a lower 1σ error bar and 84% quantile as an upper 1σ error bar—representing how many times of predicted grain sizes by slab and ISM models to the Mie grain size H_2O ice phases at different temperatures.

The inability of the slab model in predicting the 3.1 μm reflection peak of H_2O is likely due to having higher k values at these wavelengths (Hansen 2009; Mastrapa et al. 2009).

3.2. Relative Grain Size Estimation

We assess the uncertainty in the predictions of grain sizes by the Hapke approximation models for the ice phases at the investigated temperatures. A finely spaced range of grain sizes at radii of 1, 10, 100, and 1000 μm (hereafter we denote as reference grain radii) was used to show the relative discrepancies of grain size prediction at NIR wavelengths. We chose this range because it covers the grain sizes expected to be found in the outer solar system bodies. For instance, fine-grain H_2O ice with a diameter of <1 μm has been predicted on Pluto (Cook et al. 2019). Much larger grain sizes are also believed to be present in outer solar system bodies such as icy moons and rings of Saturn (e.g., Filacchione et al. 2012) and Pluto (e.g., Cook et al. 2019).

Accordingly, we first compute the δ–Eddington corrected Mie w' at these reference grain radii over the NIR wavelengths. Once the Mie w' is calculated, we determine the grain sizes from each of the Hapke approximation models that provide the best fit to the Mie spectra over the selected wavelengths. To this end, we solve the inverse of the ISM and Hapke slab model for D to fit the corresponding Mie w' values. We use the modified Powell's hybrid method (Powell 1970; Chen & Stadtherr 1981) to solve the nonlinear function of the Hapke slab and ISM (Equations (2) and (5)) in finding the solution for D. The relative grain size prediction is then determined by normalizing the predicted grain sizes by the approximation models to the reference grain radii input in the Mie model.

We estimate the medians and their 16% quantile as a lower 1σ error bar and 84% quantile as an upper 1σ error bar of predicted grain sizes using the approximation models for Ia (Table 1(a)) and Ic (Table 1(b)) at the investigated temperatures. As additional supporting information, we also list the mean $\pm 1\sigma$ standard deviation in predicted grain sizes in the Appendix (Table A1). The statistics were derived from the

normalized values of the estimated grain sizes predicted by the slab model and ISM to the Mie model. A value of 1 represents exact prediction while the higher or lower values imply an over or underestimation, respectively, of the grain sizes by the respective approximation models to the Mie model. Thus, the values in Table 1 (and Table A1) indicate the magnitude of the discrepancies in grain size prediction by the approximation models.

To facilitate visual comparisons of our result over the NIR wavelengths, we plot the normalized predicted gain size for Ia (Figure 2) and Ic (Figure 3) by approximation models at different reference grain radii and temperatures. Similar to Table 1, the y-axis value of 1 in each subplot of Figures 2 and 3 represents an exact prediction while the higher or lower values imply an over or underestimation, respectively, of the grain sizes by the approximation models to the Mie model. Thus, the y-axis values in the subplots of Figures 2 and 3 indicate the magnitude of discrepancies in predicted grain sizes at NIR wavelengths.

The discrepancies in the estimated grain sizes combining all parameters (i.e., ice phases, grain radii, temperatures, and scattering models) simultaneously are complicated, and, consequently, interpreting the result accommodating all parameters together is difficult. Thus, we analyze our result by comparing the discrepancies in predicted grain sizes within a particular parameter while keeping the rest of the other parameters constant/fixed. For instance, we first start by comparing the discrepancies in estimated grain sizes between ice phases (Ia versus Ic) predicted by the approximation models at corresponding temperature and reference grain radii.

Overall, the predicted grain sizes are much better for Ic than Ia by both approximation models, because the median values are much closer to 1 for Ic compared to Ia at the corresponding temperature and grain radii (see Table 1). In other words, between the ice phases at most of the corresponding temperatures and grain radii, both approximation models produce median values that are much better for Ic compared to Ia. As an example, for 10 μm radii at 40 K, the Ic and Ia show a median value of 1.09 versus 1.20 by the slab model, respectively, and 1.30 versus 1.45 by the ISM, respectively (Table 1). One exception in this instance is that the slab model's prediction of 1 μm radii is slightly better for Ia than Ic, such as a median value of 1.07 versus 0.88 at 60 K, respectively (Table 1). However, the corresponding 16 and 84% quantile error bars for the 1 μm grain are higher for Ia than Ic. The mean values (Table A1) between the ice phases are also mostly consistent with the median values, except for smaller grains ($\leqslant$10 μm radii) at lower temperatures ($\leqslant$40 K). Therefore, we conclude that the Hapke approximation models predict much better, in general, grain sizes for Ic than for the Ia phase. Quantitatively, the predicted grain sizes by the approximation models are roughly 10%–20% higher (on average) for Ia than Ic.

While comparing discrepancies between the approximation models for a particular ice phase, temperature, and reference grain radii, the slab model shows a better approximation (i.e., median values much closer to 1) than the ISM. This is evident from the median (except for Ic at 1 μm radii) and mean $\pm 1\sigma$ values (except Ia for 10 μm radii at 40 K) at every temperature, grain radii, and ice phase. As an example, for 10 μm radii Ia particles at 40 K, the medians are 1.20 and 1.45 for the slab model and ISM, respectively (Table 1(a)). Likewise, for 10 μm radii Ic particles at 40 K, the median value is 1.09 versus 1.30 for the slab model and ISM, respectively (Table 1(b)). Even though the median of ISM is slightly better than the slab model for 1 μm radii Ic grain (for instance, a median value of 1.03 versus 0.88 at 20 K, respectively), the 16 and 84% quantile error bars are lower for the slab model than the ISM. The mean values (Table A1) between the approximation models for both ice phases are also consistent (with only one exception) with the median values. Quantitatively, the ISM predicted grain sizes are around 10%–25% higher than the slab model's prediction for both ice phases (ignoring the exceptions). The subplots in the left and right columns of Figures 2 and 3 also support that the slab model's predictions are much better (qualitatively) than ISM at a particular ice phase, temperature, and grain radii. For instance, the 1000 μm radii curve of ISM shows much more fluctuations on the y-axis than the slab model's curve for similar grain radii at every temperature of ice phases. The higher discrepancies in grain size estimation by ISM are consistent with the result of Hansen (2009).

The discrepancies in response to temperature changes (from $\sim$15 to 80 K) indicate that the median values of both ice phases for particular grain radii by the approximate models do not substantially change in response to temperature variations (Table 1). This implies that the temperature changes within an ice phase may not have a major impact on predicting H_2O grain size using the Hapke approximation models. Unlike median values, the mean values of Ia particles by the approximation models slightly change in response to temperature. However, the change does not follow a particular pattern for most of the grain radii (Table A1). In contrast, the mean values for Ic by the slab model slightly decrease in response to temperature increase while for ISM the change does not show a particular pattern for grain radii (Table A1). Overall, the discrepancies in predicted H_2O ice grain sizes by the approximation models due to the temperature variations roughly vary $\sim$1%–5%. This is further supported by the row-wise subplots in Figures 2 and 3 which clearly show that the shapes of the different radii curves do not substantially change due to temperature changes.

The grain size prediction of the Ia phase at every temperature indicates that both approximation models produce higher median values (higher uncertainty) for larger grain radii (Table 1(a)). As an example, for an Ia particle at 60 K, the slab model predicts a median value of 1.07 and 1.55 for the 1 and 1000 μm radii, respectively, while for ISM it is 1.29 and

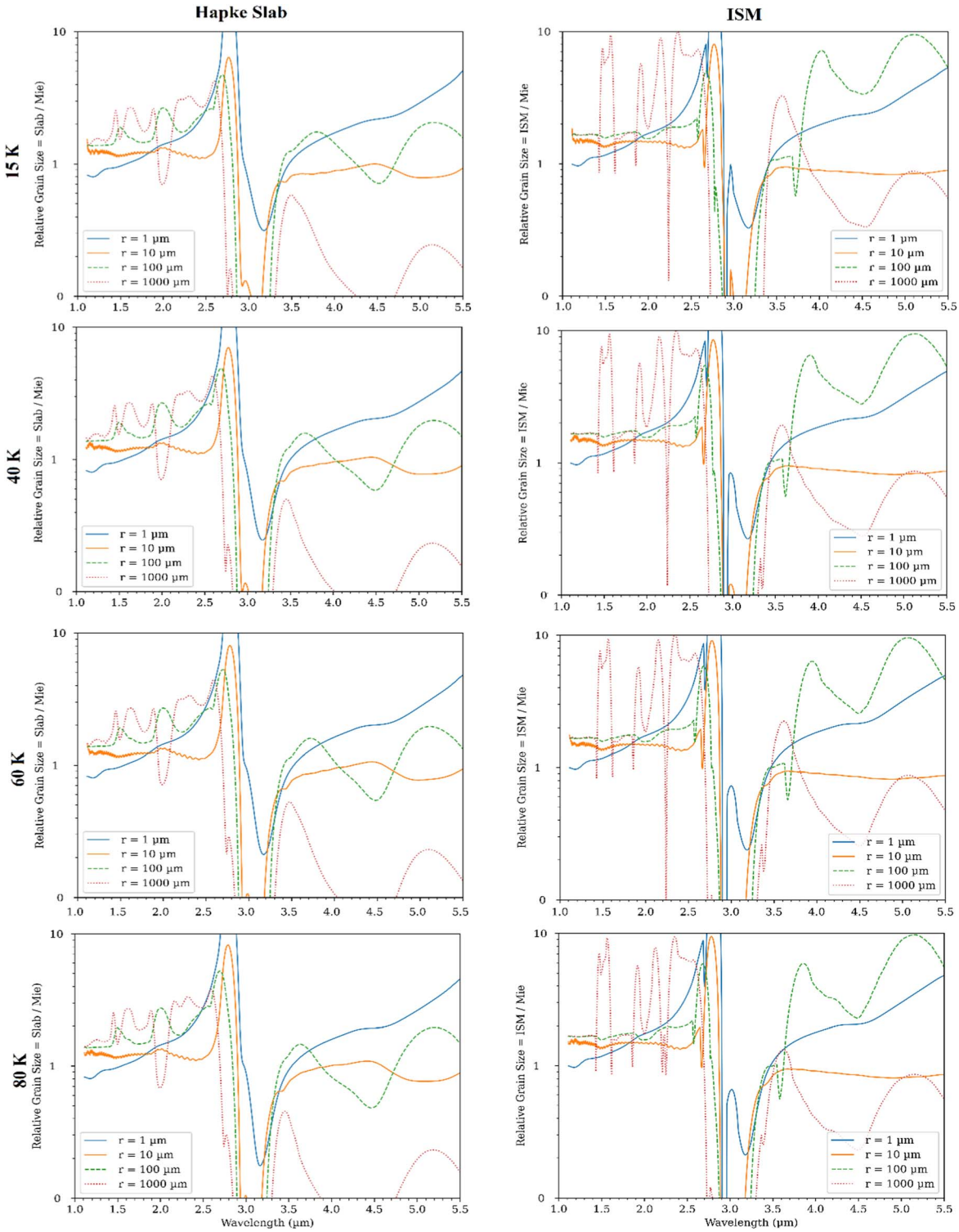

Figure 2. Predicted relative gain sizes (normalized to the Mie prediction) using the Hapke slab (left column) and ISM (right column) calculated at particle radii of 1, 10, 100, and 1000 μm for amorphous H_2O ice, for temperatures ranging between 15 and 80 K.

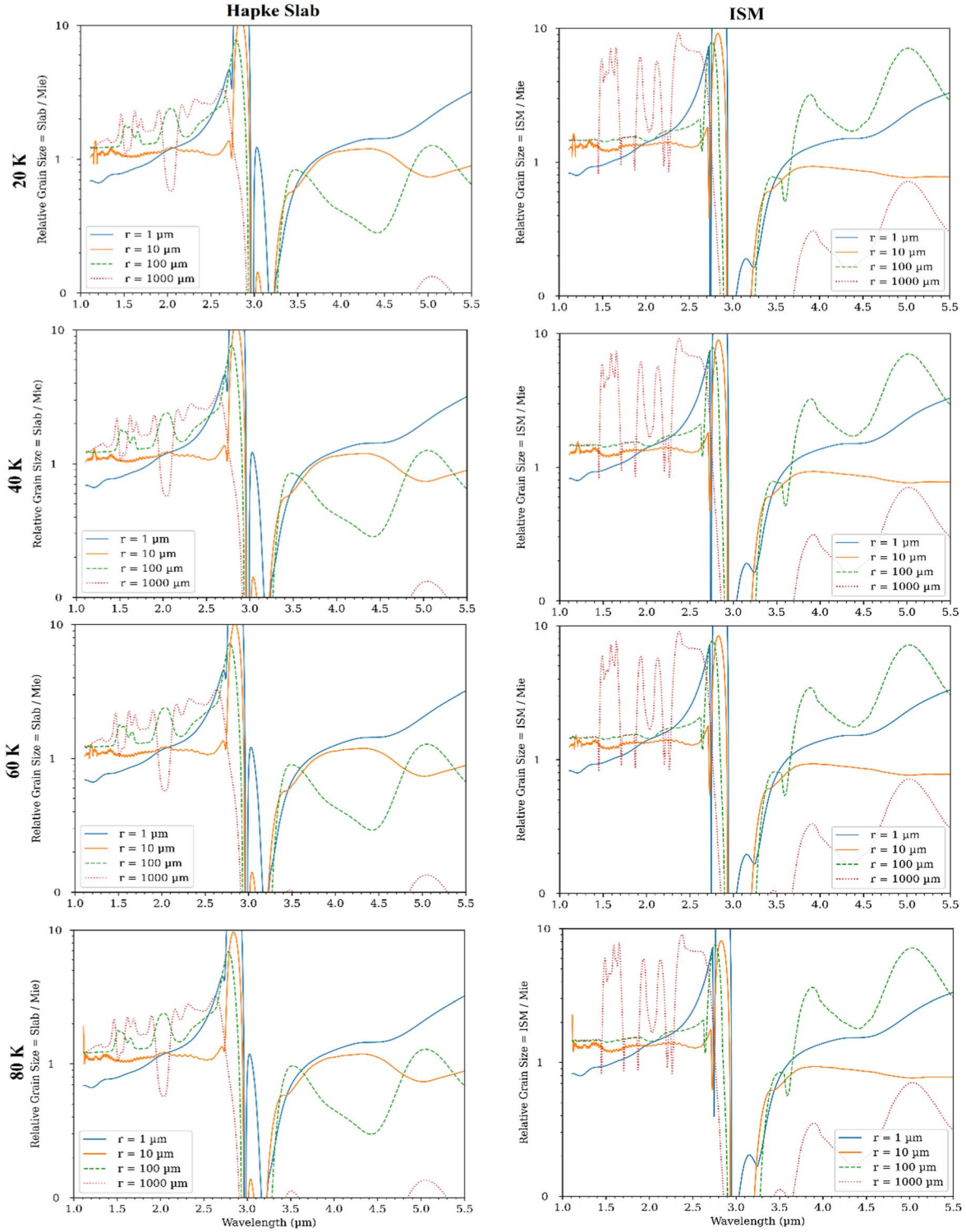

Figure 3. Predicted relative gain sizes (normalized to the Mie prediction) using the Hapke slab (left column) and ISM (right column) calculated at particle radii of 1, 10, 100, and 1000 μm for crystalline H_2O ice, for temperatures ranging between 20 and 80 K.

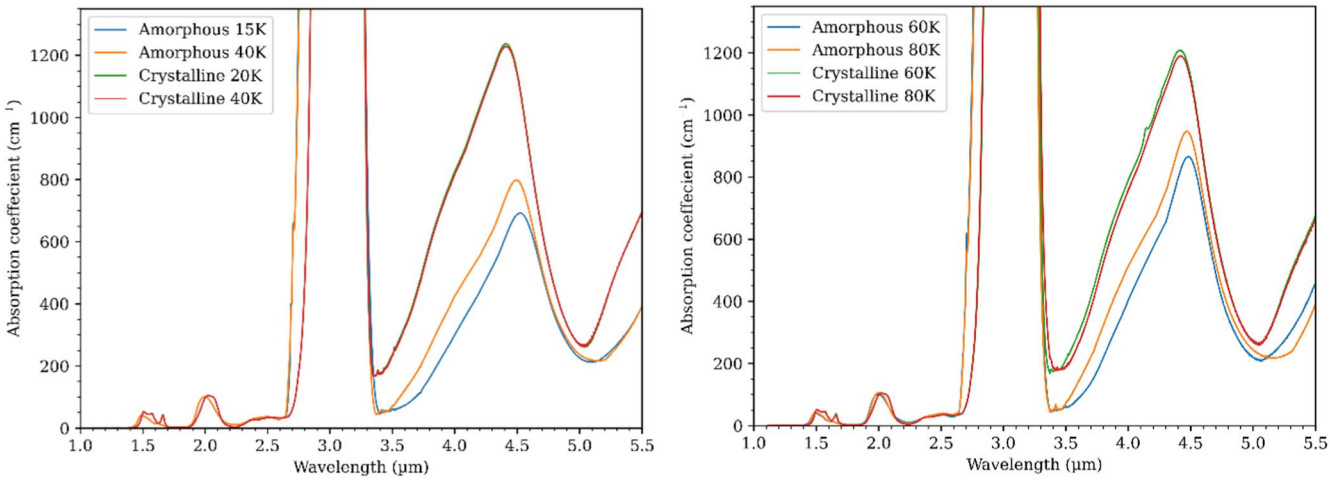

Figure 4. Absorption coefficient of amorphous and crystalline H_2O ice at different temperatures over NIR wavelengths. Both phases of H_2O have a broad absorption coefficient peak of around 3.0 μm with a little shift toward shorter wavelengths by the Ia. Another absorption peak is seen at 4.5 μm for Ia while this peak shifts toward shorter wavelengths at 4.4 for Ic with much higher α values. The higher absorption peak for Ic compared to Ia at longer wavelengths is associated with the higher k values at these wavelengths.

1.68, respectively. A similar trend is also evident for Ic particles at every temperature such that the prediction of the larger grain sizes has higher uncertainty by both approximation models (Table 1(b)). Note that the slab model's prediction of 1 μm radii Ic particles is slightly smaller than the Mie models—the median values are all less than 1. Quantitatively, the discrepancies in predicting larger grain radii by the approximation models can be up to 40%–50% of the Mie model's prediction. This effectively means that grain size estimation by both approximation models is substantially deviant from that of the Mie model's estimation in predicting larger H_2O ice grains irrespective of ice phase.

We visually compare and, subsequently, qualitatively interpret the discrepancies in predicting different grain sizes over the NIR wavelengths (Figures 2 and 3). The 1 μm radii curves (for both the ice phase and each temperature) rise continuously at shorter wavelengths up to $\sim$2.8 μm (Figures 2 and 3). This continuous rise at shorter wavelengths is largely due to the Rayleigh effect on w from the Mie model that happens at wavelengths close to or smaller than the grain size (Hansen 2009). The Hapke approximation models do not account for the Rayleigh effect. Thus, even though the median values of the 1 μm radii show a good prediction (Table 1), the mean $\pm 1\sigma$ standard deviation displays one of the highest discrepancies (Table A1). The 10 μm radii curves (for each ice phase and temperature) show a better prediction than other radii curves over the NIR wavelengths. The median values are also in agreement with the above conclusion since the medians are close to 1 (except for 1 μm radii). This is further supported by mean values for 10 μm radii which are closest to 1 (lowest discrepancy) compared to other grain radii.

Though the 100 μm radii curves by the ISM show relatively less fluctuation around the value 1 on the y-axis at shorter wavelengths than the slab model, at longer wavelengths ($>$3 μm) this behavior is the opposite. Consequently, the 100 μm radii curves by the slab model overall exhibit values much better than the ISM's prediction for both ice phases at each temperature. The 1000 μm radii curves by the slab model for both ice phases show much larger fluctuations on the y-axis among the other radii curves in Figures 2 and 3—which explains why they have the highest median values among the grain radii. However, the corresponding 1000 μm curve by ISM produces much higher discrepancies.

For larger particles ($\geqslant$100 μm radii) at each ice phase and temperature, the approximation models predict much smaller grain sizes at longer wavelengths (above 3.5 μm) than Mie's prediction (Figures 2 and 3). A possible reason for smaller grain size prediction is that the approximation models do not reproduce the characteristic higher saturation level of the Mie model (Hansen 2009). For both ice phases, the fluctuation of the 1000 μm radii curves by ISM at shorter wavelengths is even much higher than the 1 μm radii curve, where there is a continuous rise of the curves due to the Rayleigh effect (see the right columns in Figures 2 and 3). In both ice phases, the mean and median values by the ISM for the 1000 μm radii are the largest among all corresponding values (Tables 1 and A1).

3.3. Characteristic Absorption Coefficient

To explain the effect of absorption coefficient in grain size prediction, we plot the dependency of the α on wavelength (following Equation (3)) for both ice phases and temperatures (Figure 4). At each temperature, both phases exhibit a

maximum value of α at the wavelengths close to 3.0 μm, although with a slight shift toward shorter wavelengths for ice Ia compared to ice Ic. The higher absorption peak at 3.0 μm (orders of magnitude higher α values than at other wavelengths) is due to the higher k values (the imaginary part of the optical constant) at these bands. This renders gain size prediction impossible by the approximation models—also evident at 3 μm wavelengths in Figures 2 and 3. This result supports the assumption that the slab model should be used if $k \ll 1$ (Hapke 1981). A blueshift in α spectra of Ia compared to the Ic phase is also evident at the weak 2 μm band, which coincides with the fact that Ic is much stronger, sharper, and redshifted at infrared bands than Ia (Schmitt et al. 1998).

Higher values of α are also seen at the longer wavelengths for both ice phases. However, a peak of α happens at around 4.5 μm for Ia while this peak shifts toward shorter wavelengths at 4.4 for Ic—in agreement with Mastrapa et al. (2009). The effects of these α peaks are evident in the characteristic shapes (i.e., a dip) in grain radii curves at these wavelengths for larger particles (i.e., 100 and 1000 μm; Figures 2 and 3). The relatively higher α value at 4.5 μm for Ic compared to Ia is apparent in the curve of the 1000 μm particle (Figures 2 and 3) where the Ic reveals a higher discrepancy in grain size prediction than the Ia for both approximation models at the wavelength.

The α of pure CH_4 and N_2:CH_4 (N_2 saturated with CH_4) systems, the other abundant volatile ices found on KBOs and TNOs surfaces, at NIR wavelengths (see Figure 3 of Emran & Chevrier 2022) have a much lower α than water ice phases. A simple interpretation of this fact is that the H_2O ice may have higher absorption and lower reflectance compared to the pure CH_4 and N_2:CH_4 ices on the TNOs (e.g., Triton) and KBOs (e.g., Pluto, Eris, and Sedna). However, this interpretation may not be true amid different other factors involved with spectral signatures of the ices, particularly in an ice mixture. The results above show that the higher discrepancies in predicated grain sizes for larger particles are largely aligned to the wavelengths with higher α values. Accordingly, the estimation of H_2O ice grain size using the Hapke approximation models for larger particles may be susceptible to higher uncertainty than that of CH_4 and N_2:CH_4 ices at the Kuiper Belt (Emran & Chevrier 2022).

The α of Ia at the 4.5 μm absorption band (and slightly at 1.5 and 2 μm bands) increases with changes in temperature from 15 to 80 K (Figure 4). This α versus temperature characteristic of Ia may likely be the cause of the slightly higher discrepancy in grain size prediction than the Mie model's prediction with the higher temperatures at these bands (Figure 2). In contrast, Ic does not show any substantial variation in α values with temperature at the 4.4 μm absorption band, although α slightly decreases with temperature increase. Therefore, in the case of Ic, there are no substantial differences in grain size estimations at this wavelength between each temperature (Figure 3).

4. Discussion

We use the Hapke models for predicting grain sizes of 1 μm radii even though the approximation model assumes that the particle size should be much larger than the wavelengths (Hapke 1981). This study uses wavelengths close to or even larger than grain radii of 1 μm. Alternatively, we also test a more conventional scenario with a wide range of grain sizes much larger than the considered wavelengths. The rationale for using 1 μm radii is based on reports of the presence of H_2O ice with similar sizes on the surface of outer solar system bodies like KBOs (e.g., Cook et al. 2019). Moreover, the use of a 1 μm grain size emphasizes the Rayleigh effect that happens at grains that have sizes close to NIR wavelengths often used to study the composition of outer solar system planetary surfaces (e.g., Hansen 2009; Emran & Chevrier 2022). And by taking smaller particle sizes, we evaluate the grain size prediction discrepancies at wavelengths close to or even larger than the grain size of 1 μm radii. On top of that our result shows how deviant, as expected, grain size prediction from the approximation models can be—compared to Mie (Figures 2 and 3)—when the wavelengths are close to or even larger than the grain size.

The predicted grain sizes by the Hapke approximation models vary over the investigated wavelengths due to the optical constants (and, therefore, different absorption coefficient values) at different NIR bands and the formulation of the approximation models used (see Equations (2) and (5)). In simple words, the approximation models predict different grain sizes based on optical constant values ($n + ik$) at different wavelengths. This scenario may also be in line with recorded laboratory spectra, where absorption coefficients can change with grain size, along with ice phase, temperature, etc. (Clark 1981; Singh 2021). Accordingly, assessing the predictions of these varying grain sizes at different wavelengths by the approximation models to Mie theory was the motivation of the study and, thus, we evaluate the discrepancies in predicting varying grain sizes by the scattering models. As mentioned above, we only consider the optical constant of cubic crystalline ice as a generalization of crystalline ice. However, there are only subtle differences in spectra between the cubic and hexagonal phases (Bertie & Whalley 1967), and, thus, we emphasize that the crystalline phases are substitutable (Mastrapa et al. 2009) and the use of Ic for generalization of the crystalline ice is reasonable.

Between the ice phases, the grain size estimation for Ic applying the Hapke approximation models result in a much closer, in general, estimate to Mie's prediction. Conversely, the Hapke approximation models show higher discrepancies from Mie's prediction of grain size estimation for Ia. The variation in temperature within a phase does not have much influence on average grain size estimation at NIR wavelengths. However, grain size estimation for larger Ia particles at longer wavelengths reveals a pattern such that the discrepancy in

grain sizes increases with temperatures from 15 to 80 K. In contrast, the discrepancies in grain size estimation of larger Ic particles at longer wavelengths are negligible between the temperature range. Interestingly, grain size estimation for larger particles at the broad 4.4–4.5 μm absorption band leads to a higher discrepancy for Ic compared to Ia. Overall, the relative discrepancies of the grain size estimation are better for the Hapke slab model than ISM at the investigated cryogenic temperatures. This indicates Hapke slab results in a much closer approximation to Mie's estimate for deriving the water ice grain sizes in the icy bodies of the outer solar system. Our result is consistent with the results previously analyzed by Hansen (2009) using the optical constant of Ic at a temperature of 110 K.

Owing to the Rayleigh effects on single scattering albedo, neither of the approximation models predicts accurate grain size estimation results for the particles with diameters less than or close to the wavelengths ($\leqslant 5$ μm). For both Ia and Ic, grain size estimations for 10 μm radii H_2O ice are best predicted by both Hapke approximation models to the Mie model's prediction. Though grain size prediction by the approximation models for larger radii shows higher discrepancies largely at the wavelengths with higher absorption coefficient values, the uncertainty in the instance of ISM is much higher than in the Hapke slab model. The higher discrepancies of grain size estimation for larger particles by ISM can be compromised by adjusting the free parameters used in calculating single scattering albedo, for instance, the study of Roush et al. (2007) used a higher value of s to fit modeled spectra.

While formulating the "*espat*" function for the slab model, Hapke (1981) used a scaling factor of $\hat{g} = 2/3$ for particle diameter. However, the scaling factor of diameter in the Hapke slab model varies between $3/4$ and $4/3$ which can, in principle, result in a difference in grain size estimation by the slab model (Hansen 2009). Likewise, the difference in grain size estimation by ISM can also be produced by scaling factor to the particle diameter by calculating the mean free path of the photon $\langle D \rangle$ as seen in Equation (7). There have been different approximate expressions for the relationship between D and $\langle D \rangle$. This relationship is approximated as $\langle D \rangle \cong 0.9D$ or $2D/3$ (e.g., Hapke 2012; Melamed 1963) for spherical particles while it is $\langle D \rangle = 0.2$ D for irregular particles (Shkuratov & Grynko 2005). Hence, the grain size estimation by the approximation models can be improved by carefully adjusting the scale factor for particle diameters. We use a scale factor of 1 for the slab model while the mean free path of a photon in ISM was calculated as a function of the diameter and real part of the refraction index.

While both Hapke approximation models do not account for the Rayleigh effect on the single scattering albedo that happens to grain sizes close to the wavelengths ($\leqslant 5$ μm), the Mie theory appropriately accounts for this shortcoming. Though the rough average difference between the predicted grain sizes by the ISM and slab model is about $\sim$10%–25% (based on the median values in Table 1) for a wide range of particles, we emphasize that it is still an over/underestimation by one approximation model to another while comparing with the Mie model's result. Our study also shows which approximation model predicts much better results which approximate Mie's predictions in estimating the grains sizes of Ia and Ic found in the vast region of the outer solar system.

A closer prediction of H_2O ice grain sizes of Mie's estimation by the slab model than ISM is also in agreement with the grain size estimation of the abundant surface volatile of N_2 and CH_4 ices on TNO and KBO surfaces (Emran & Chevrier 2022). Thus, the Hapke slab model is better equipped to mimic the Mie model for the implementation of RTMs in grain size estimation for a range of surface ices (H_2O, N_2, and CH_4) in the outer solar system bodies. We recommend using the Mie formulation of the single scattering albedo for estimation of H_2O ice (Ia and Ic) grain sizes for unknown spectra of outer solar system bodies. When choosing the approximation models, we recommend using the Hapke slab model over ISM since our result presumes that the slab model better approximates the H_2O grain size prediction of Mie, overall, than the ISM at 1–5 μm wavelengths.

The single scattering albedo may not be readily available from the measurements of spacecraft observations. However, the reflectance (or radiance coefficient) measurements by spacecraft observation are converted to single scattering albedo using the RTM such as Hapke (1993). Conversion of reflectance (r_c) measurement from remote sensing observation to single scattering albedo (w) using the Hapke (1993) model requires other parameters of the RTM to be known or calculated. Of these the important parameters are observation geometry (i.e., incident (i), emission (e), and phase (g) angles), single scattering phase function ($P(g)$), backscattering function (B(g)), and multiple scattering functions (H, for both up-welling and down-welling radiance; (e.g., Lawrence & Lucey 2007; Mustard & Glotch 2019). The parameters related to observation geometry (*i, e,* and g) come directly with remote sensing reflectance (or radiance) measurements while other parameters can be approximated using the appropriate equations given in Hapke (1981, 1993, 2012).

Conversion of remote sensing reflectance to single scattering albedo is crucial for deriving the material abundance and grain size of planetary regolith using RTMs. Because it is predicated that a linear mixing of regolith components for an intimate mixture is only reasonable if a single scattering albedo is converted from reflectance (e.g., Mustard & Glotch 2019). Thus, the implementation of RTMs to estimate grain size involves first the conversion of remote sensing reflectance (r_c) measurements to single scattering albedo (w), followed by the implementation of a linear fitting (least squares or other minimization routine) algorithm to estimate the abundance and grain size of surface components. The linear fitting algorithm

assumes that the average w of a planetary regolith is a linear combination of the w of a plausible set of endmembers present in the mixture systematic weighted by each endmember's relative geometric cross-section (e.g., Mustard & Glotch 2019). The w spectra of the endmembers are calculated from their optical constant data such as, in this instance, amorphous and crystalline H_2O ice for the outer solar system.

Ultimately, therefore, an estimation of the grain size of the surface components in the outer solar system bodies through the implementation of the RTM feeds on single scattering albedos spectra—both from remote sensing observations and plausible endmembers. Hence, the predicted grain sizes of planetary surface components (e.g., H_2O ice) using RTMs ought to be affected by the differences in the estimated single scattering albedo spectra (i.e., remote sensing observation and endmembers) and, inherently, the methods used to derive endmembers' single scattering albedo from their optical constants. This is further supported by Hansen (2009) who argued and showed that the variations in the estimation of H_2O grain sizes at Saturnian moons are attributed due to the differences in single scattering albedo calculation rather than the bidirectional scattering model. Accordingly, we assess the discrepancies in grain size estimation of H_2O ice in the outer solar system owing to the implementation of a variety of widely used scattering models (Mie and Hapke approximations) in the existing literature.

Despite having concerns related to the validity of the models and uncertainty in the parameters involved (e.g., Mustard & Glotch 2019), the RTMs have been widely utilized and successfully implemented in estimating the grain size of a wide range of planetary regolith in the solar system including terrestrial and icy surfaces (e.g., planets, asteroids, moons, etc.). Note that in remote sensing observations, the single scattering albedos are the calculated properties of a planetary surface using the RTM rather than being directly measured. In Hapke's formulation of RTM, the single scattering phase function ($P(g)$) and single scattering albedo (w) are closely associated such that if $P(g)$ is smaller in the direction of the observer's remote sensing instrument, a larger w can compensate, and vice versa (Hapke 1993). Thus, a variation in $P(g)$ estimation can influence the calculation of w and, consequently, can influence the prediction of grain size. However, the discrepancies in the estimation of grain size of H_2O ice due to variation in different single scattering phase functions ($P(g)$) is beyond the scope of the present study. In this study, our focus was rather to assess how the implementation of a variety of the widely used scattering models can render the variation of w calculations and resultant discrepancies in H_2O grain sizes, how much the variations are, and based on the results of these variations what is the most appropriate method in what situation.

5. Conclusion

The mechanical strengths and thermal properties of planetary surfaces are directly influenced by the grain size of planetary regolith (e.g., Gundlach & Blum 2013). Thus, an accurate grain size estimation of the outer solar system bodies is very important for an improved understanding of the surface volatile transport and thermophysical modeling of the planetary bodies. The icy bodies in the outer solar system host a widespread presence of water ice on their surfaces. Understanding the grain sizes of planetary regolith supports both landing or sample return missions (Gundlach & Blum 2013), and thus accurate information about the water ice grain sizes is crucial for future missions to the outer reaches of the solar system.

We assess the discrepancies in the grain size estimation of amorphous and crystalline H_2O ice at cryogenic temperatures from 15 to 80 K at a $\sim$20 K interval. The relative grain size prediction by the Hapke approximation models to Mie's theory was assessed, both quantitatively and qualitatively, concerning ice phases, grain sizes, and temperatures analogous to the icy zones of the solar system. Having a satisfactory application of Mie theory to an equant as well as "equivalent" non-spherical particles, we recommend using Mie formulation for unknown spectra of the outer solar system bodies. However, if approximation models are preferred, our study suggests applying the slab model rather than the ISM.

We demonstrate which approximation model works better in predicting grain size estimated by the Mie theory for the water ice found in the outer solar system. Incorporating the results from Emran & Chevrier (2022), we conclude which approximate model is better in predicting the grain sizes estimated by Mie for a variety of surface ices found in the outer solar system bodies, specifically on TNOs and KBOs. Thus, this study put forward a guideline for future studies in choosing scattering models in estimating the water ice grain sizes in the outer solar system using the RTMs at NIR bands.

Acknowledgments

The authors would like to thank Samuel Cano, Abhilash Ramachandran, and anonymous reviewers for their useful comments. The paper used Python packages including NumPy (Harris et al. 2020), SciPy (Virtanen et al. 2020), MatplotLib (Hunter 2007), and MiePython https://pypi.org/project/miepython/).

Appendix A
Statistics

The mean and $\pm 1\sigma$ standard deviation of relative discrepancies in grain sizes are predicated by the approximation models.

Table A1
The Statistics—mean and $\pm 1\sigma$ Standard Deviation—of Relative Discrepancies in Predicted Grain Sizes Using the Hapke Slab and ISM Calculated at Particle Radii of 1, 10, 100, and 1000 μm for Amorphous (a) and Crystalline (b) H_2O ice at Different Temperatures

a.

Grain radii (μm)	Amorphous H_2O ice[a]							
	15 K		40 K		60 K		80 K	
	Slab	ISM	Slab	ISM	Slab	ISM	Slab	ISM
1	1.89 ± 3.06	2.07 ± 2.96	1.96 ± 3.42	2.25 ± 4.13	2.08 ± 3.97	2.43 ± 5.14	2.11 ± 4.10	2.44 ± 5.22
10	1.21 ± 0.74	1.40 ± 0.92	1.23 ± 0.82	1.14 ± 0.98	1.26 ± 0.95	1.42 ± 1.06	1.27 ± 0.98	1.43 ± 1.10
100	1.58 ± 0.72	2.05 ± 1.62	1.57 ± 0.75	2.06 ± 1.59	1.59 ± 0.80	2.04 ± 1.57	1.59 ± 0.81	2.06 ± 1.59
1000	1.51 ± 1.00	2.62 ± 2.44	1.51 ± 1.02	2.57 ± 2.47	1.52 ± 1.03	2.58 ± 2.48	1.50 ± 0.99	2.41 ± 2.29

b.

Grain radii (μm)	Crystalline H_2O ice[a]							
	20 K		40 K		60 K		80 K	
	Slab	ISM	Slab	ISM	Slab	ISM	Slab	ISM
1	2.07 ± 5.76	2.19 ± 5.99	2.05 ± 5.64	2.17 ± 5.89	1.97 ± 5.15	2.13 ± 5.62	1.97 ± 5.15	2.13 ± 5.62
10	1.24 ± 1.35	1.32 ± 1.08	1.24 ± 1.30	1.31 ± 1.05	1.22 ± 1.20	1.30 ± 0.99	1.22 ± 1.20	1.30 ± 0.99
100	1.44 ± 1.05	1.74 ± 1.25	1.44 ± 1.04	1.74 ± 1.24	1.43 ± 0.99	1.75 ± 1.26	1.43 ± 0.99	1.75 ± 1.26
1000	1.28 ± 0.86	2.30 ± 2.21	1.27 ± 0.85	2.31 ± 2.21	1.27 ± 0.84	2.31 ± 2.22	1.22 ± 0.84	2.31 ± 2.22

Note.
[a] The statistics were computed by normalizing the estimated grain sizes from the Hapke slab and ISM to the Mie grain size. The number values are the mean and $\pm 1\sigma$ standard deviation—representing how many times of predicted grain sizes by slab and ISM models to the Mie grain size H_2O ice phases at different temperatures.

Appendix B
Notation

List of notation and symbols used in this paper
$B(g)$ backscattering function
$\langle D \rangle$ mean free path of a photon
D particle diameter
D_e effective particle sizes
e emission angle
ξ asymmetry parameters of Mie theory
g phase angle
$\hat{g}$ a constant, roughly $= 1$
H multiple scattering function
i incident angle
k imaginary part of the refractive index
n real part of the refractive index
$P(g)$ phase function
r internal diffused reflectance
r_c reflectance or radiance coefficient
s internal scattering coefficient
S_e Fresnel reflection coefficient for externally incident light
S_i Fresnel reflection coefficient for internally incident light
w single scattering albedo
w' δ–Eddington Mie single scattering albedo α
absorption coefficient λ
wavelength Θ
internal transmission coefficient

ORCID iDs

A. Emran https://orcid.org/0000-0002-4420-0595
V. F. Chevrier https://orcid.org/0000-0002-1111-587X

References

Baragiola, R. A. 2003, P&SS, 51, 953
Barucci, M. A., & Merlin, F. 2020, The Trans-Neptunian Solar System (Amsterdam: Elsevier), 109
Bertie, J., & Whalley, E. 1967, JChPh, 46, 1271
Chen, H.-S., & Stadtherr, M. A. 1981, Comput. Chem. Eng., 5, 143
Clark, R. N. 1981, JGRB, 86, 3087
Cook, J. C., Dalle Ore, C. M., Protopapa, S., et al. 2019, Icarus, 331, 148
Cruikshank, D. P., Roush, T. L., Owen, T. C., Quirico, E., & Bergh, C. D. 1998, Solar System Ices (Berlin: Springer), 655
Cruikshank, D. P., Schmitt, B., Roush, T. L., et al. 2000, Icarus, 147, 309
Dalle Ore, C. M., Protopapa, S., Cook, J., et al. 2018, Icarus, 300, 21
Dumas, C., Merlin, F., Barucci, M., et al. 2007, A&A, 471, 331
Earle, A. M., Binzel, R. P., Young, L. A., et al. 2017, Icarus, 287, 37
Emran, A., & Chevrier, V. 2022, AJ, 163, 196

Emran, A., Dalle Ore, C., Ahrens, C., et al. 2023, PSJ, 4, 24
Filacchione, G., Capaccioni, F., Ciarniello, M., et al. 2012, Icarus, 220, 1064
Grenfell, T. C., Neshyba, S. P., & Warren, S. G. 2005, JGRD, 110, 15
Grenfell, T. C., & Warren, S. G. 1999, JGRD, 104, 31697
Grundy, W., & Schmitt, B. 1998, JGRE, 103, 25809
Grundy, W. M., & Fink, U. 1991, Icarus, 93, 379
Gundlach, B., & Blum, J. 2013, Icarus, 223, 479
Hansen, G. 2009, Icarus, 203, 672
Hansen, G. B., & McCord, T. B. 2004, JGRE, 109, 19
Hapke, B. 1981, JGRB, 86, 3039
Hapke, B. 1993, Theory of Reflectance and Emittance Spectroscopy: Topics in Remote Sensing (Cambridge: Cambridge Univ. Press)
Hapke, B. 2012, Theory of Reflectance and Emittance Spectroscopy (Cambridge: Cambridge Univ. Press),
Harris, C. R., Millman, K. J., Van Der Walt, S. J., et al. 2020, Natur, 585, 357
Herbst, E. 2001, Chem. Soc. Rev., 30, 168
Hudgins, D., Sandford, S., Allamandola, L., & Tielens, A. 1993, ApJS, 86, 713
Hunter, J. D. 2007, CSE, 9, 90
Joseph, J. H., Wiscombe, W., & Weinman, J. 1976, JAtS, 33, 2452
Kofman, V., He, J., ten Kate, I. L., & Linnartz, H. 2019, ApJ, 875, 131
Lawrence, S. J., & Lucey, P. G. 2007, JGRE, 112, 18
Li, S., & Li, L. 2011, JGRE, 116, 14
Lucey, P. G. 1998, JGRE, 103, 1703
Mastrapa, R., Bernstein, M., Sandford, S., et al. 2008, Icarus, 197, 307
Mastrapa, R., Sandford, S., Roush, T., Cruikshank, D., & Dalle Ore, C. 2009, ApJ, 701, 1347
Melamed, N. 1963, JAP, 34, 560
Merlin, F., Barucci, M., de Bergh, C., et al. 2010, Icarus, 208, 945
Mie, G. 1908, AnPhy, 330, 377
Mustard, J. F., & Glotch, T. D. 2019, Theory of reflectance and emittance spectroscopy of geologic materials in the visible and infrared regions, in Remote Compositional Analysis: Techniques for Understanding Spectroscopy, Mineralogy, and Geochemistry of Planetary Surfaces, ed. J. L. Bishop, J. F Bell III, & J. E. Moersch, Vol. 21 (Cambridge: Cambridge Univ. Press)
Neshyba, S. P., Grenfell, T. C., & Warren, S. G. 2003, JGRD, 108, 4448
Powell, M. J. 1970, A hybrid method for nonlinear equations, in Numerical Methods for Nonlinear Algebraic Equations, ed. P. Rabinowitz (London: Gordon and Breach), 87
Protopapa, S., Grundy, W., Reuter, D., et al. 2017, Icarus, 287, 218
Raponi, A., Ciarniello, M., Capaccioni, F., et al. 2016, MNRAS, 462, S476
Roush, T. L. 1994, Icarus, 108, 243
Roush, T. L., Esposito, F., Rossman, G. R., & Colangeli, L. 2007, JGRE, 112, 17
Savitzky, A., & Golay, M. J. 1964, AnaCh, 36, 1627
Schmitt, B., Quirico, E., Trotta, F., & Grundy, W. 1998, Solar System Ices (Berlin: Springer), 199
Sharkey, B. N., Reddy, V., Sanchez, J. A., Izawa, M. R., & Emery, J. P. 2019, AJ, 158, 204
Shepard, M. K. 2017, Introduction to Planetary Photometry (Cambridge: Cambridge Univ. Press),
Shepard, M. K., & Helfenstein, P. 2007, JGRE, 112, 17
Shkuratov, Y. G., & Grynko, Y. S. 2005, Icarus, 173, 16
Singh, V. 2021, PhD thesis, Arizona State Univ.
Tegler, S. C., Cornelison, D., Grundy, W., et al. 2010, ApJ, 725, 1296
Virtanen, P., Gommers, R., Oliphant, T. E., et al. 2020, NatMe, 17, 261
Wiscombe, W. J. 1979, Mie Scattering Calculations: Advances in Technique and Fast, Vector-speed Computer Codes, 10 (Alexandria, VA: National Technical Information Service, US Department of Commerce)
Wiscombe, W. J. 1980, ApOpt, 19, 1505
Wiscombe, W. J., & Warren, S. G. 1980, JAtS, 37, 2712